10-20-2021

A Reduced-Order Lumped Model for Li-Ion Battery Packs during Operation

Paul T. Coman
University of South Carolina, comanpt@cec.sc.edu

Eric C. Darcy

Brad Strangways

Ralph E. White
University of South Carolina, white@cec.sc.edu

Publication Info
Published in *Journal of Electrochemical Society*, Volume 168, 2021.

OPEN ACCESS

A Reduced-Order Lumped Model for Li-Ion Battery Packs during Operation

Journal of The Electrochemical Society, 2021 **168** 100525

A Reduced-Order Lumped Model for Li-Ion Battery Packs during Operation

Paul T. Coman,[1,*,z] Eric C. Darcy,[2] Brad Strangways,[3] and Ralph E. White[1,]**

[1]*Department of Chemical Engineering, University of South Carolina, Columbia, South Carolina 29208, United States of America*
[2]*NASA Johnson Space Center, Houston, Texas 77058, United States of America*
[3]*Symmetry Resources Inc., Arab, Alabama 35016, United States of America*

Modeling heat distribution in Li-ion battery packs can be challenging, especially if the battery pack is large and the cells are operated at high C-rates, which usually requires high-order physics-based mathematical models. Reduced and simplifying models can, however, be used at lower rates. This paper presents a fast novel reduced lumped model (RLM) that can be used to calculate the temperature increase during the high-current discharge of cylindrical Li-ion cells in a subscale of a battery pack. By reducing the PDE utilized to calculate the state of charge (SoC) to ODE's and solving them analytically, the reduced model can be a very reliable and fast tool for calculating the temperature distribution in battery packs. The voltage was calculated by considering the charge overpotential, the ohmic overpotential, and the activation overpotential, while the properties of the parameters are dependent on the temperature following an Arrhenius-dependency. Comparing with experimental data, the model showed a good prediction of the temperature readings showing good potential in using the model for battery packs operating at high C-rates (>2 C).

 [DOI: 10.1149/1945-7111/ac2dcb]

Manuscript submitted June 28, 2021; revised manuscript received August 25, 2021. Published October 20, 2021.

Lithium-ion battery cells are critical components for pushing the technology towards electrical mobility, whether talking about electric vehicles, airplanes, volocopters, or even space applications. Building battery packs is an engineering art, and choosing the suitable cell chemistries and geometries for specific load profiles in different ambient is a big challenge. A battery management system (BMS) can be developed for a battery pack that helps balance the cells' potentials, can measure/predict the temperature and feedback on different key parameters such as the State of Charge (SoC), but the CPU of the BMS and the controller speed can be a limiting factor, mainly if the BMS code is based on complex electrochemical or electrical models. It is, therefore, crucial to find different methods to decrease the modeling and code complexity while increasing the computational speed and keeping a high precision.

Mathematical models are powerful tools that can be converted and deployed to controller code (such as C code) and thus implemented in BMS. Such modeling tools were developed over the years by scientists and consist of reducing full-order models (FOM) to reduced-order models (ROM) for single cells, which can significantly increase the computation speed while keeping a high precision. One of the most popular and relievable FOMs used for reducing reduction is the classical Newman's model, a physics-based pseudo-2D model based on the porous electrode theory.[1–4] Newman's model was proven to give a suitable temperature and voltage prediction for various cell chemistries and geometries even at high operating rates (over 1C-Rate), which is very appealing for converting to ROMs. Over the years, different mathematical methods for modeling reduction were explored, such as domain decomposition and polynomial approximation methods,[5] Padé approximation and polynomial fitting combined with volume averaging techniques,[6] residue grouping methods,[7] Kalman filtering,[8] or using transfer functions,[9] among others. Most of them are reliable, in general. Some extended or improved ROMs (eROM's and iROM's) can predict the voltages and SoC even at high C-rates. However, the level of complexity for reducing and implementing these models, in addition to the high number of parameters required for a P2D model, makes them less likely to be implemented in the BMS's at the current development stage.

Another method is to use other first-principle simplified FOM's derived from the P2D with the assumptions that some of the gradients in the electrodes can be neglected, such as the Single Particle Model (SPM) and its derivatives such as Extended Single Particle Model (ESPM).[10,11] Reduction of SPM models was also made using methods such as the Galerkin approximations, quasi-linearization, etc.[12,13] Xiaoyu Li et al.[13] found that the latter approach gives very high accuracy in predicting the voltage and the temperature even at high rates while improving the computation time. But even reduced FOM's such as the SPM requires some measured parameters which are not only easy to extract or measure (such as the diffusion coefficient for both the anode and the cathode). Other modeling methods requiring fewer parameters while accurately predicting the potentials are so-called lumped models, which are dimensionless. An example of such a model is the equivalent circuit model (ECM).[14] This method has been used extensively in the research literature and real-life applications. It was used both in single cells and in the BMS of battery packs or coupled with many other physics such as fluid dynamics.[15–20] The ECM, although fast and reliable in many cases at low rates, lacks a mechanistic and physical interpretation of the phenomena inside the cells.

Another recent lumped model that showed a remarkable potential was semi-empirical and included some physical interpretation when calculating the overpotentials.[21] The model was developed by Henrik Ekström, Björn Fridholm, and Göran Lindbergh and has proven to show great promise when compared its predictions of a hybrid electric vehicle (HEV) driving load cycle. The model requires a minimal number of fitting parameters and consists of a single PDE applied to a one-dimensional particle for calculating the SoC and different formulations for calculating the overpotential, including a kinetic expression defined as an inverted Butler-Volmer equation. The lumped model was later reduced using Laplace transformation and transfer functions by Benjamin Ng et al.[22] It was shown that a one-step reduced lumped model (consisting only of ODEs) can be anchored to experimental data and can predict both the temperature and the voltage at different rates. The challenge, however, is to demonstrate if such a model can predict the temperature in a battery pack and further implemented it in a BMS. This paper thus introduces a novel reduced lumped model used for modeling the temperature rise in a subscale of a battery pack. The particular model

*Electrochemical Society Member.
**Electrochemical Society Fellow.
[z]E-mail: COMANPT@cec.sc.edu

was further reduced by solving the ODE's, and the core model parameters were defined as temperature-dependent functions.

Battery pack thermal models have been developed by many authors over the years. Coupling between electrochemical models and thermal models, CFD or structural models, have been done in many different creative and inter-disciplinary ways, using various methods such as genetic algorithms,[23] machine learning,[24] and ordinary 2D or 3D FEM or internal thermal networks models.[25,26] For a heat transfer or even thermodynamic analysis of a battery pack, and simulate the temperature rise in each cell, it is essential to formulate the heat generation rate term or the total energy. Few methods have been used throughout the years to determine such a formulation and couple with an electrochemical model. One of the most comprehensive and accurate methods was given by Thomas and Newman,[27] which comprises of an irreversible resistive heating term, a reversible entropic heat term, the heat capacity, a heat change due to residual or side chemical reactions, and a heat of mixing term, as follows:

$$\dot{Q}_{gen} = \overbrace{\left(\overbrace{IV - \sum_1 I_1 U_1^{avg}}^{\text{irreversible}}\right)}^{} + \underbrace{\sum_1 I_1 T \frac{\partial U_1^{avg}}{\partial T}}_{\text{reversible}} + \overbrace{C_p \frac{dT}{dt}}^{\text{specific heat}} + \underbrace{\sum_1 \Delta H_k^{avg} r_k}_{\text{side reaction}} + \overbrace{\int \sum_j \sum_i (\overline{H}_{ij} - \overline{H_{ij}^{avg}}) \frac{\partial c_{ij}}{\partial t} dv}^{\text{heat of mixing}}$$

The disadvantage of this formulation consists in the presence of many unknown parameters which require higher-order models. It was also demonstrated in many studies that a simplified and fast forward approach for many battery systems is to use only the heat generation given by the irreversible resistive heating term and, in some cases, with the reversible entropic term.[27,28]

$$\dot{Q}_{cell} = (IV_{cell} - IU_{cell}) + IT\frac{\partial U_{cell}}{\partial T} \quad [1]$$

The current term, I, can be taken directly from the experimental data or, with some artifices, expressed in terms of current density. The current density for a full-cell can be calculated using the so-called NTGK model (Newman, Tiedemann, Gu, and Kim[2,29,30]). The current density can also be stated as a function of temperature to include the Seebeck effect.[31] With this in mind, the model presented in this paper consists of a reduced novel lumped model with a simplified heat generation term that can be used to model the temperature rise in a subscale of a battery pack.

Experimental

To demonstrate the reduced lumped model (RLM) value, a subscale of a battery pack was chosen, as seen in Fig. 1.

Although the selection of a subscale is not a critical part of this study, it is important to show the source of it and point at the fact that subscales are an effective way to analyze the contribution of different components in battery packs (such as air gaps, cell spacing, boundary conditions, etc). It has the main advantage that it is easy to build a physical model anchored to a mathematical model without sacrificing too much precision. Subscaling of full-scale systems, although not always easy and straightforward, was used in many of the battery packs built in-house at NASA and UofSC and by other scientists, such as Vishnu V. Ganesan and Ankur Jain,[32] for example. The system presented in Fig. 1 consists of many components that are not explained in detail in this paper but can be read out in Eric Darcy et al.[33] This particular full-pack consisted of two decks populated by 96 cells (12s8p). The cells were attached with an epoxy layer to the aluminum (AL6061) heat sinks (depicted with turquoise color in the figure), transporting the heat from the cells to the top and bottom headers. The headers were connected to a metallic casing in which two cooling channels are embedded on both sides (top and bottom). The subscale consists of eight cells connected electrically to a battery cycler system that was set to discharge the cells at a constant current (CC) of 9.6 A. In this case, the subscale model assembly, test setup, and test execution were performed by Symmetry Resources, Inc.

The experimental set-up is described in detail in Fig. 2.

Eight SAMSUNG INR18650–30Q cells were glued on edge with a 1.52 mm layer of epoxy (2216 Gray 3 M™ Scotch-Weld™ Epoxy) to the aluminum AL6061 heat sink shown in Fig. 2a, forming a 90° contact angle between the cells and the heat sink, and were fitted with G10 cover plates at both ends of the cells (Fig. 2b). The cells were then wrapped outside with Kapton tape and electrically connected in series with spot-welded nickel connectors. One end of the heat sink was then attached to a mounting plate, as seen in Fig. 2c. The 8-cell assembly was covered all around with 6 mm thick durette felt insulation and wrapped with Kapton tape to reduce the heat loss. The assembly was then mounted on a cooling plate that was set to keep a constant 25 °C. (Fig. 2d). The entire sides and top of the subscale was wrapped once more with a 13 mm thick layer of PE foam insulation (Fig. 2e). The top of the mounting plate and the cold plate were also insulated, as seen in Fig. 2e. A set of thermocouples were attached to the heat sink and the cells located as shown in Fig. 3.

Four thermocouples were placed on the cells steel cans of cells 1–4, and four were inserted inside four boreholes ($\phi 1 \times 4.2$ mm) drilled in the heat sink at mid-hight to capture the temperature gradient inside the cells, as seen in Figs. 3 and 2a. Two thermocouples were placed in the vicinity of the cold plate: one drilled at the interface between the heat sink and the mount plate and another one drilled in the mounting plate to a position adjacent to the heat sink interface thermocouple. These two thermocouples are crucial for aiding the thermal model, as explained in the next sections.

Modeling work

The reduced model was based on the lumped model presented by Henrik Ekström et al.[21] and was reduced to ODE's using the methods suggested by Benjamin Ng et al.[22] The lumped model originally developed in Refs. 21 and 22 is a semi-empirical model which yields a time-dependent formulation for the cell voltage based on the difference between the open circuit voltage and the over-potentials due to the linear ohmic resistance, a non-linear charge transfer resistance and a diffusion impedance. The SoC of the cell was calculated using a PDE in Ref. 21 and then reduced to an ODE in Ref. 22 (see the derivation in appendix A in Ref. 22). The model was initially demonstrated in Ref. 21 to predict a load cycle consisting of current pulses (ranging between the maximum of −240 A and 100 A) of different rates for a NMC cell (24.8 Ah). This indicates that the lumped model can predict the voltage for rates higher than 1–2C-Rate, which can be a limiting rate for other models such as the Single Particle Model.

The model presented in this paper is reduced even further, from ODE's to AE's, by solving the ODE's analytically. Additionally, some of the parameters are defined to be dependent on the temperature. To demonstrate the importance of the lumped model, it was coupled with a Finite Element Thermal Model using COMSOL Multiphysics v5.6. A simplified 3D geometry of the subscale was chosen (see the dimensions in Table A·1), as seen in Fig. 4a.

In this geometry, the G10 cover plates were disregarded, as it was found that they didn't have a solid contribution to the thermocouple readings on the sides, which were of high interest for this particular study. Also, adding the G10 would have overcomplicated the model and significantly increased the computation time. The ratio between its thickness and the width and length is very large, which would have added a tremendous number of mesh nodes.

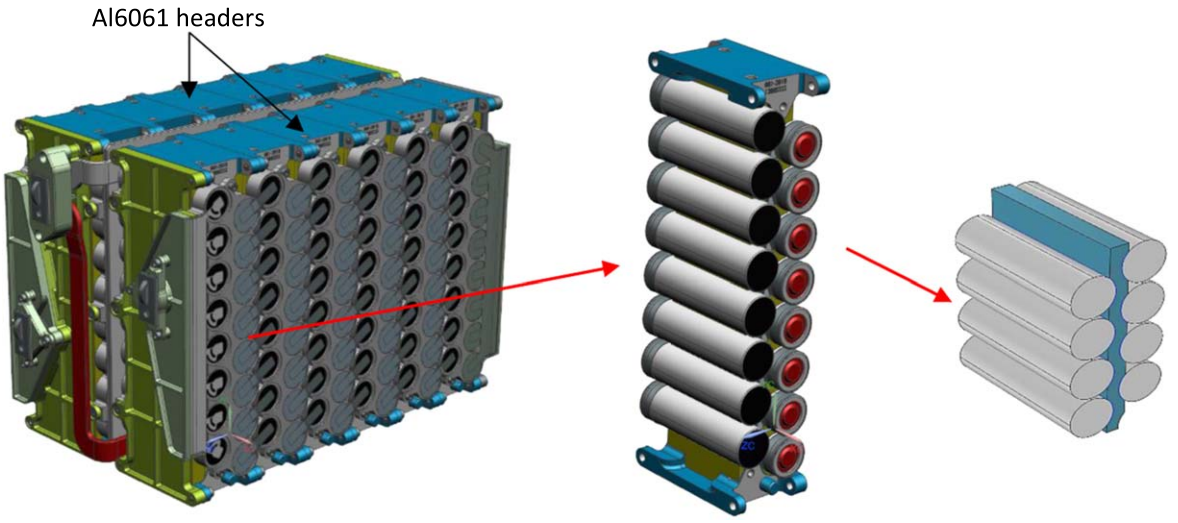

Figure 1. Sketch showing the method of selection for singling out the subscale (used as a system for the model).ictures showing different building steps of the experimental set-up for the pack subscale.

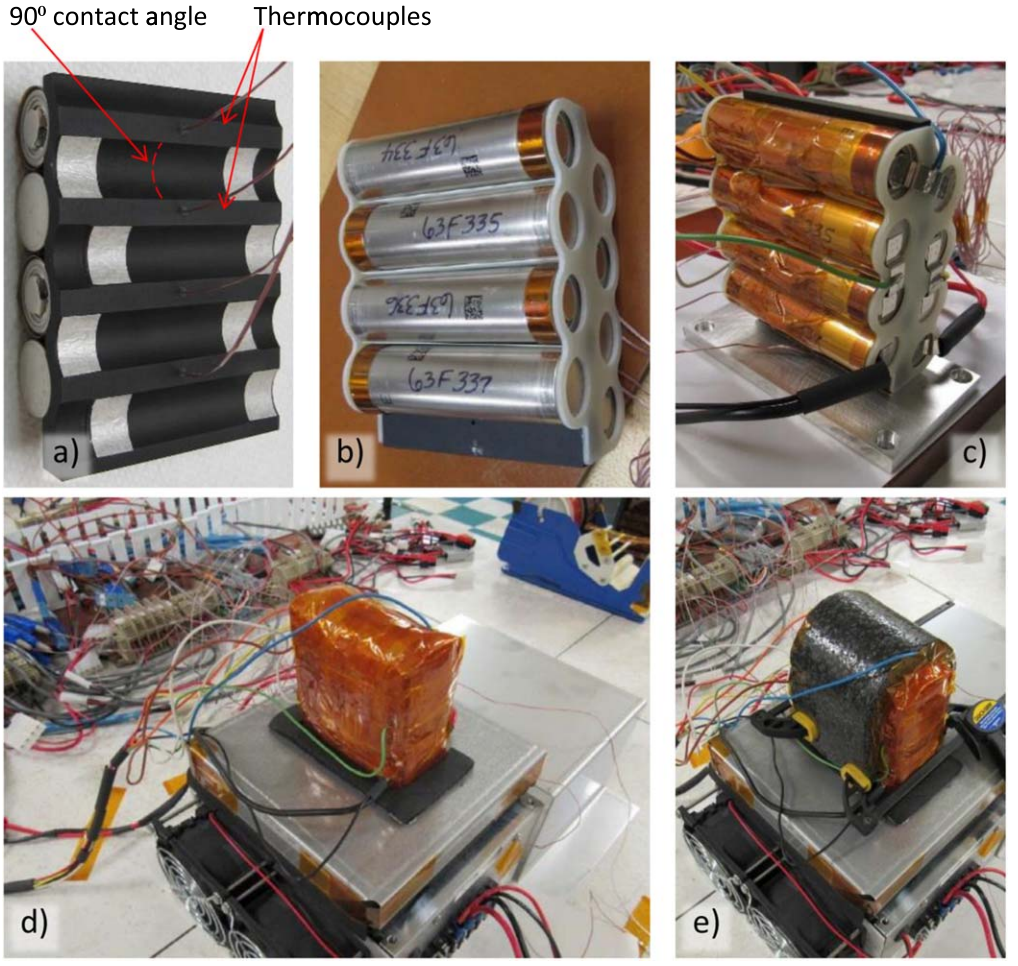

Figure 2. Pictures showing different building steps of the experimental set-up for the pack subscale.

At the top, where the heat sink was connected to the cold plate, surface temperature boundary conditions (BCs) were assigned (Fig. 4b), and the temperature was time-dependent and extracted from experimental data. The thermocouple measurement drilled close to that boundary (see Fig. 3) was proven to be extremely useful in setting up this BC. The boundary conditions on the faces in contact with the Kapton tape and the insulation blanket (Fig. 4c) were assumed to be fully insulated (adiabatic conditions). Each cell domain had assigned a volumetric heat generation term ($\dot{Q}_{\text{cell}}$) that was calculated using the RLM (Fig. 4c) and added to the heat equation expressed in Cartesian coordinates for each thermal anisotropic cell domains:

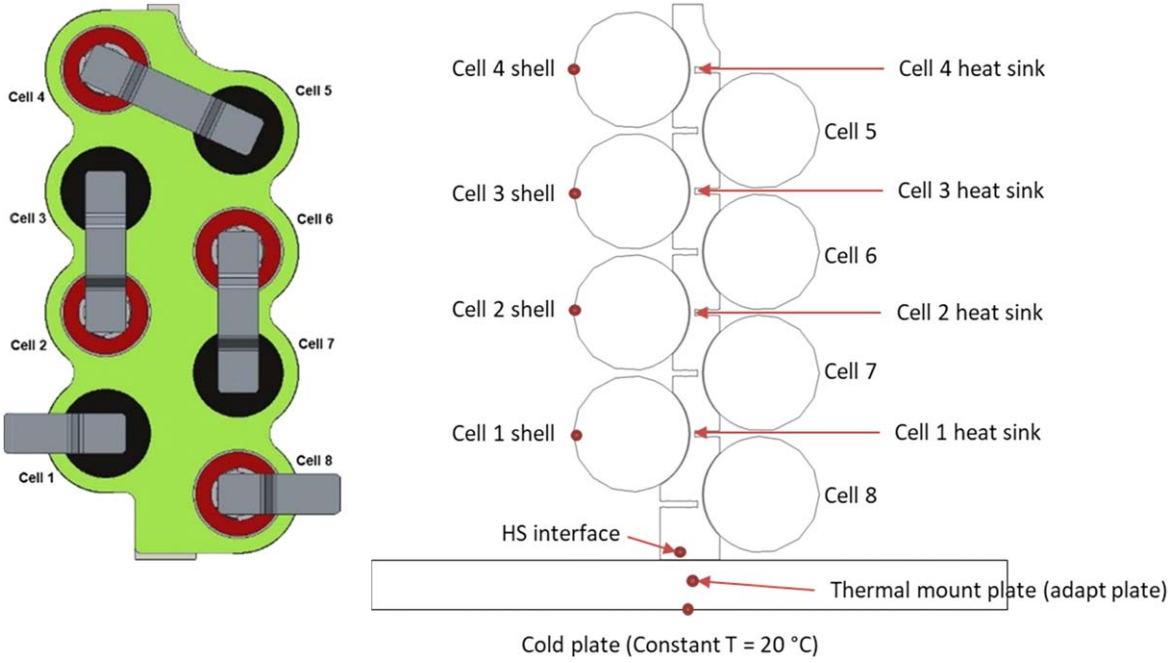

Figure 3. Sketch showing the 3D geometry (to the left) and the 2D mid-section, indicating the position of the thermocouples used to measure the temperature. The dimensions in holes in the heat sink are $\phi 1 \times 4.2$ mm, and they have very little influence on the heat transfer within the heat sink.

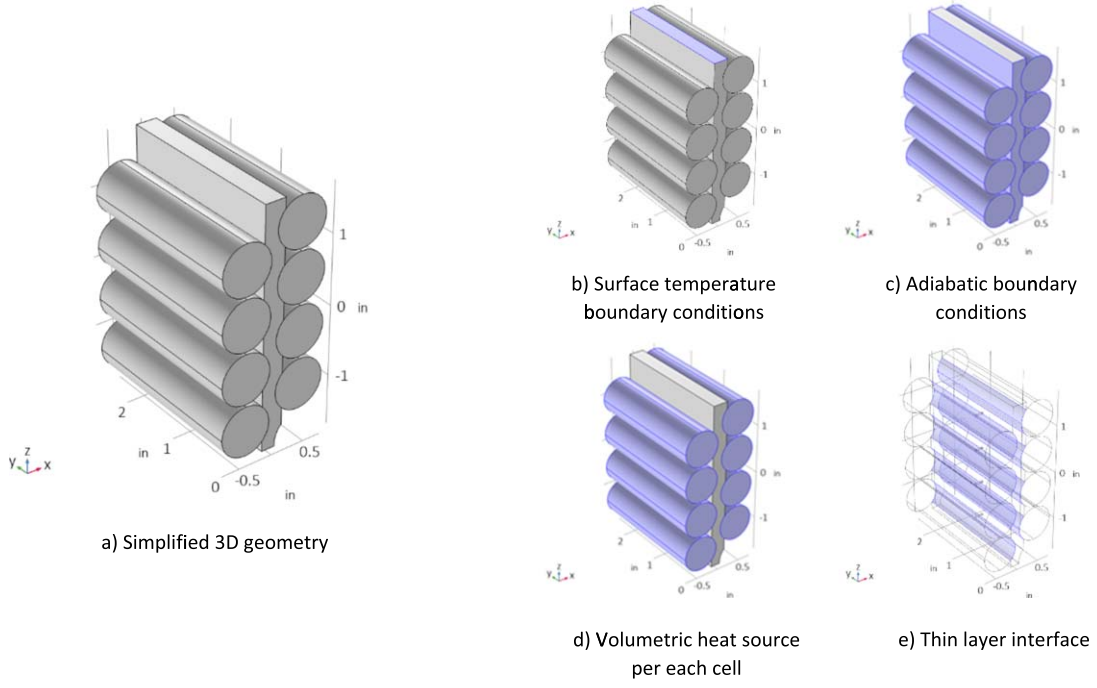

Figure 4. Simpified geometry used for the thermal model and the corresponding boundary conditions. The geometry view is flipped (cold plate connection is at the top) for better visualization of the boundary conditions.

$$\rho_{eff} C_{p,eff} \frac{\partial T}{\partial t} = \frac{\partial}{\partial x}\left(k_x \frac{\partial T}{\partial x}\right) + \frac{\partial}{\partial y}\left(k_y \frac{\partial T}{\partial y}\right) + \frac{\partial}{\partial z}\left(k_z \frac{\partial T}{\partial z}\right) + \dot{Q}_{cell} \quad [2]$$

The density (ρ_{eff}) and the heat capacity ($C_{p,eff}$) of the cell domains are effective values, while the thermal conductivities are anisotropic (the radial k_x and k_z are different than the axial k_y). The values are taken from Ref. 34 for a single 18650 cell with an electrolyte and given in Table I.

The 0.5 mm epoxy layer between the cells and the heat sink can be modeled in two ways.

1. Adding meshed domain, which would add thousands of extra meshing nodes and significantly increasing the computation cost while requiring complex meshing operations.

Table I. Optimized parameter values in approximated transfer function.

Parameter	Value	Parameter	Value
a_1	35058.7	b_1	−268.261
a_2	1382.966	b_2	−30.9242
a_3	141.595	b_3	−7.59606
a_4	22.32279	b_4	−2.59525

2. Taking advantage of COMSOL's "Thin Layer" feature, which can be applied to a boundary between two domains.

The latter was proven to be extremely useful in thin layers, both in Ref. 35 and in the COMSOL documentation,[36] and was therefore used in this study.

For calculating the volumetric heat generation term ($\dot{Q}_{cell}$) using the formulation from Eq. 1, the RLM was developed. The formulation for calculating the average state of charge can be calculated as:

$$\frac{dSoC_{avg}}{dt} = \frac{I}{Q_{actual}} \quad [3]$$

Solving analytically, yields:

$$SoC_{avg} = \frac{It}{Q_{actual}} + SoC_0 \quad [4]$$

The SoC at the surface of the particles can be calculated using the reduction method shown in Benjamin Ng et al.[22] using the technique presented originally in Ref. 37. $SoC_{surface}$ is defined in terms of an eigenfunction as a series:

$$SoC_{surf} = SoC_{avg} + \sum_{i=1}^{N=4} F_i \quad [5]$$

Where the eigenfunction F_i is given as:[22]

$$\frac{dF_i}{dt} = \frac{q_i F_i}{\tau_T(T)} + \frac{b_i I}{Q_{actual}} \quad [6]$$

Solving analytically, yields:

$$F_i = -\frac{(Ib_i\tau_T(T) - Ib_i\tau_T(T)e^{-\frac{a_i t}{\tau_T(T)}})}{3Q_{actual}a_i} \quad [7]$$

where τ is defined as a function of temperature, expressed as in Eq. 14. In a real system, the initial State of Charge (SoC_0) and the actual capacity is temperature and rate dependent. For simplicity and for this particular demonstration, these parameters were kept constant, however, they can also be expressed as a function of temperature using an Arrhenius formulation or even using the specs for the SAMSUNG INR18650–30Q cells. The terms a_i and b_i are the optimized parameter values in approximated transfer function given in Table I, as optimized and given originally in Ref. 37.

With algebraic definitions of the average SoC and the surface SoC, the cell potentials and the overpotentials can be calculated:

$$V_{cell} = U_{cell} + \eta_{IR} + \eta_{act} + \eta_{conc} \quad [8]$$

The Open Circuit Voltage (denoted with U_{cell}) is given as:

$$U_{cell} = U(SoC_{avg}) + (T - T_{ref})\frac{dU(SoC_{avg})}{dT} \quad [9]$$

The OCV depends both on the SoC and on the temperature and requires careful experimental measurements. The dependency on the temperature was neglected in this study. The effect of temperature on the OCV can be substantial in some cases, especially when needing to increase the precision of the temperature curves, as shown in Refs. 22, and 28 but can also be neglected at low rates and low SoC, as shown in Ref. 38. Neglecting it will induce some differences in the temperature profiles but will be discussed in detail in the Results section. In this model, the OCV is defined as the OCV measured experimentally:

$$U_{cell} = U(SoC_{avg}) \quad [10]$$

The OCV was measured experimentally as a function of the state of charge. The OCV was measured after one hour of rest and discharge of C/20 in 5% capacity increments. The measured OCV was then compared with the data from the literature for a similar cell. Both OCV's have very similar profiles, as can be seen in Fig. 5.

The overpotentials can be calculated as:[21]
Ohmic overpotential (η_{IR}):

$$\eta_{IR} = \frac{\eta_{1CT}(T)I}{I_{1C}} \quad [11]$$

Activation overpotential (η_{act}):

$$\eta_{act} = \frac{2RT}{F}\text{asinh}\left(\frac{I}{2J_{0T}(T)I_{1C}}\right) \quad [12]$$

Concentration overpotential (η_{conc}).

$$\eta_{conc} = U(SoC_{surf}) - U(SoC_{avg}) \quad [13]$$

As seen from Eqs. 6, 7, 10, and 11, some of the parameters (τ_T, η_{1CT}, and J_{0T}) were defined as a function of temperature, which is another figure of merit for this RLM. The ohmic overpotential (η_{IR}), which is caused by the change in the internal resistance, is dependent on the temperature. That is, at higher temperature, the internal resistance decreases.[40] The activation (interfacial kinetics) overpotential (η_{act})

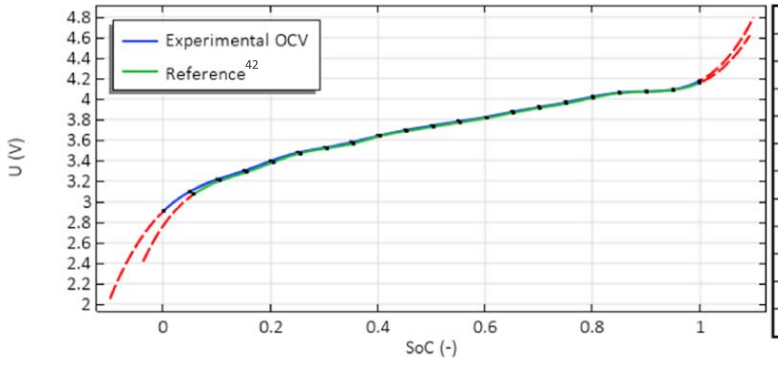

SoC	U	SoC	U
0	2.911	0.55	3.783
0.05	3.104	0.6	3.824
0.1	3.215	0.65	3.877
0.15	3.3	0.7	3.923
0.2	3.396	0.75	3.969
0.25	3.477	0.8	4.025
0.3	3.526	0.85	4.065
0.35	3.578	0.9	4.077
0.4	3.641	0.95	4.096
0.45	3.697	1	4.181
0.5	3.742		

Figure 5. Comparison between the OCV measured experimentally as a function of SoC (blue) and the OCV from Ref. 39.

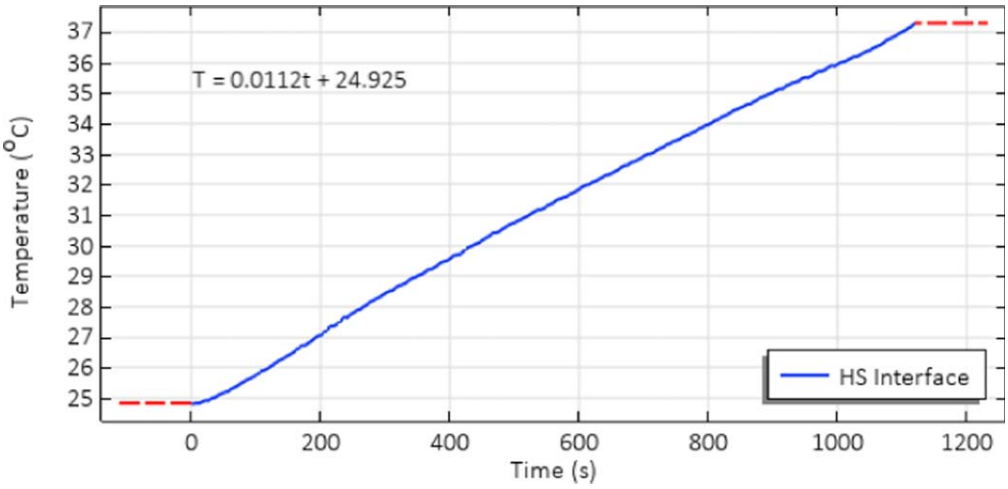

Figure 6. Plot showing the temperature increase measured experimentally at the interface between the cold plate and the heat sink (in point "HS interface" in Fig. 3) and the linear trendline approximation.

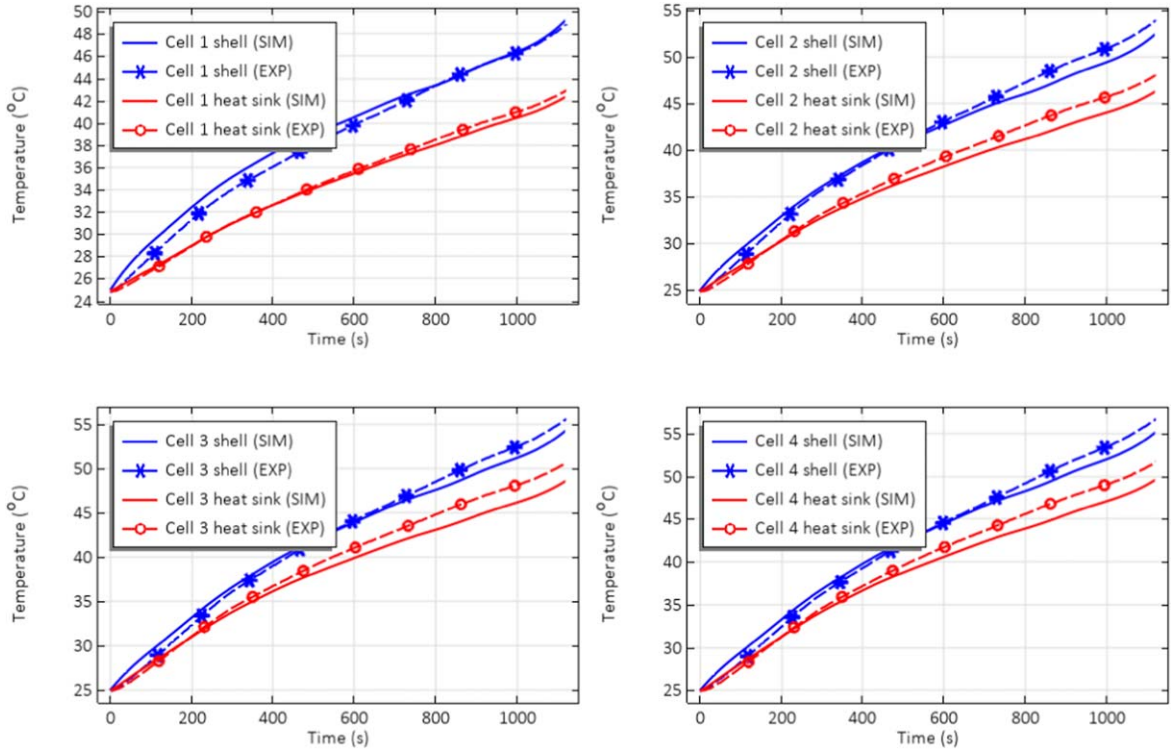

Figure 7. Plots showing the comparison between the model predictions and the experimental data for different thermocouple readings.

is also dependent on the temperature. At higher temperatures, the kinetic activity occurs faster. The concentration (species transport) overpotential is also dependent on the temperature as it reflects the concentration gradients inside the electrodes.

The dependency of some parameters to temperature can be done using an Eyring formulation or Arrhenius. In this paper, an Arrhenius temperature dependency was used, as follows:[41,42]

$$Y_T = Y_{ref} e^{\frac{Ea_Y}{R}\left(\frac{1}{T}-\frac{1}{T_{ref}}\right)} \quad [14]$$

These equations were implemented for each cell domain from Fig. 4d to obtain a voltage profile for each cell using Eq. 8 and use it in the heat generation equation (Eq. 2). The temperature term (T) in each of the equations above is calculated in each node of the domain mesh, although it could be averaged over the entire domain, as shown in Ref. 35 for faster calculations.

Results

As stated previously, one important boundary condition is the surface temperature one, which is at one end of the heat sink (the surface that would be connected to the cold plate via the mounting plate). The temperature at the interface between a cold plate, for example, and the heat sink is a critical parameter that affects the cooling capacity's performance. It was observed in many in-house experiments that keeping a constant temperature (or a slight gradient) at that interface is very difficult, even if thermal grease or other interface high-conductive materials are used. It is a bottleneck for many designs, and it plays an important role,

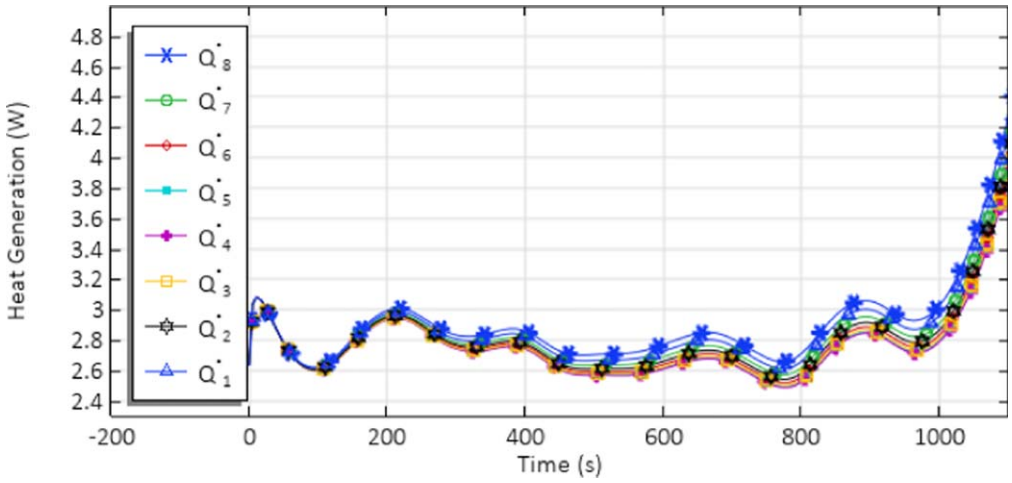

Figure 8. Plot showing the heat generation rates for each cell in the subscale.

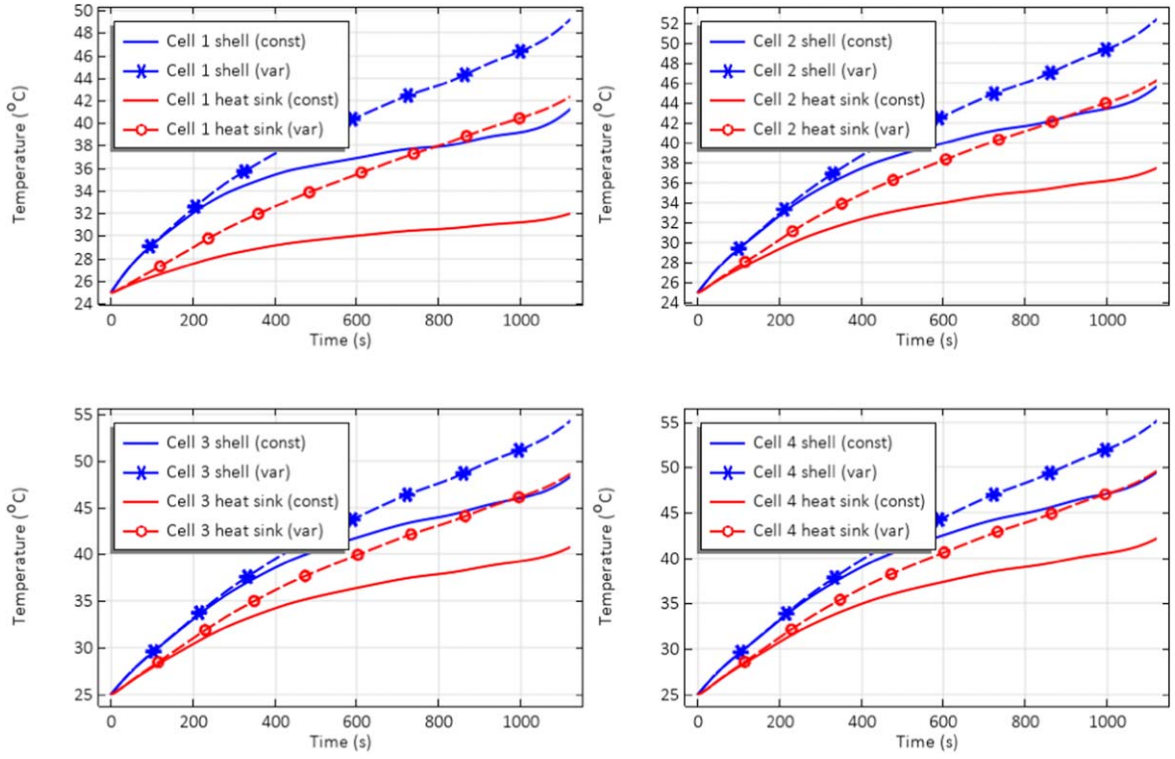

Figure 9. Plots showing the comparison of the temperatures of the cells when the cold plate interface is kept at a constant temperature of 25 °C (indicated with const in the legend) vs when the temperature is ramped, as seen in Fig. 6 (indicated with var in the legend).

especially when the contact area is small (which is the case in most of the battery pack designs that are kept cold with a cold plate). The temperature point (denoted with "HS interface" in Fig. 3) ramped up from 25 °C to 37 °C during the experiments, as seen in Fig. 6.

The solutions for solving this particular design problem are many, but it is beyond the scope of this paper; therefore, the temperature profile measured experimentally (Fig. 6) was used as the surface temperature boundary condition. With a temperature ramp at the boundary condition, adiabatic conditions at the exterior, and a heat generation calculated using the novel RLM, the model was able to predict all the temperatures measured on the surface of the cells and inside the heat sink boreholes, as seen in Fig. 7.

By looking at Fig. 7, it can be seen that the model predicts the experimental data very well, with some differences of a maximum of 2K in the cells that are further away from the cold plate (Cells 3 and 4). The temperature profiles have slightly different profiles, and one of the reasons can be the lack of including the entropic term (the reversible term in Eq. 1). By looking at the heat generation rates for each cell, it can be seen from Fig. 8 that the cell-to-cell difference in the heat generation rate between each cell in the subscale is slight. Despite this, due to the parameters' temperature dependence, the model reveals that the cells closer to the heat sink (the cold cells) have a slightly higher heat generation curve, which is expected since colder cells have a higher internal resistance.

The heat generation profiles in Fig. 8 would also have a slightly different profile if the reversible term would be added, but such a study is beyond the scope of this paper. For the 30Q cells, the energy released by the cells at 9.6A is approximately 3.2 kJ. Having an RLM that can estimate the thermal energy released at different rates and cell configurations can help calculate the waste energy by

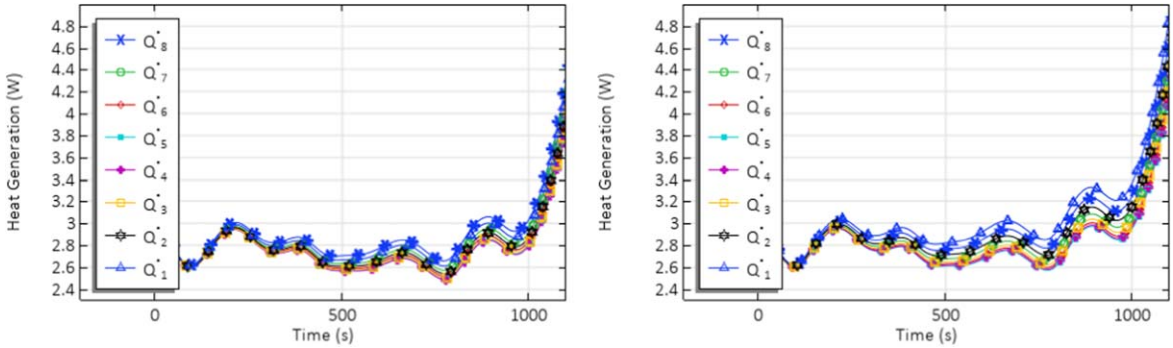

Figure 10. Plots showing a) the heat generation for the case when the temperature boundary condition was variable (see Fig. 6) and b) the heat generated when the temperature boundary condition was constant 25 °C.

dividing the heat energy estimated with the model by the electrical energy (calculated using the nominal voltage and the capacity). To further take advantage of the model capabilities, one additional study has been added to show the effect of constant temperature at the boundary (Fig. 9).

It can be seen from Fig. 9 that at a constant mount plate temperature, the difference between the heat sink and the cell shell is higher than when the temperature at the mount plate is ramped. One of the reasons is that the cells are colder and therefore generate more heat, which can also be observed in Fig. 10.

In addition to the fact that the heat generation is generally higher in the entire pack, there is also a higher cell-to-cell difference, as shown in Fig. 10b.

Conclusions

Developing reduced-order models is extremely important as they can very soon be used in battery management systems, which are currently based mainly on Equivalent Circuit Models. The RLM presented in this paper has the advantage of being very fast and easy to implement. It contains only algebraic equations (reduced from a PDE and ODE's) that can be transformed into machine code and then implemented into BMS. The RLM was used to demonstrate that it can predict the temperature of different cells inside a subscale of a battery pack connected to a cold plate. The differences in the temperature between the model predictions and the experimental data were tiny (<2K). Furthermore, having parameters that are dependent on temperature following an Arrhenius dependency formulation, it was shown that the heat generation rate calculated for each cell emulates the physical interpretation of the phenomena inside the cells at different temperatures.

Strengths and Limitations

Even though the RLM was proven to be a powerful tool for the particular set-up/subscale presented in this paper, there are some limitations. Although significantly smaller than the number of fitted parameters required for a FOM P2D model, the number of fitted parameters is still high and does not have an experimental method to be extracted experimentally (such as the activation energies in the Arrhenius temperature-dependency formulation). However, when properly fitted, the model can predict the temperature and the heat generation in different cells inside a battery pack with high precision. The model can also be valuable when different cell or pack configurations are to be studied, and the effect of adding, changing, or removing layers (such as the epoxy layer) is to be analyzed. Another important limitation of the RLM is given by the fact that good experimental data is crucial for fitting the parameters. In more complex battery packs where the temperatures are high with large cell-to-cell gradients, there will be a need for good experimental data at different temperatures to determine the activation energies in the Arrhenius formulations. However, once fitted, the RLM can be used to calculate temperature-dependent heat generations which can be used in the heat equation for each cell for further thermal modeling and analysis of different design features, such as the influence of airgaps, different layers or the thickness of heat sinks or other design elements.

Appendix

Table A·I. List of parameters used in the model.

Parameter	Value	Unit	Description	References
r_{cells}	$9.144 \cdot 10^{-3}$	m	Radius of the cells	Measured
H_{cells}	$6.5 \cdot 10^{-2}$	m	Height of the cells	Measured
$\eta_{1C,ref}$	$3.0 \cdot 10^{-2}$	V	Ohmic overpotential at 1 C pre-exponential factor	Fitted
T_{ref}	298.15	K	Reference temperature	Measured
Ea_{eta1C}	$24 \cdot 10^{3}$	J mol^{-1}	Ohmic overpotential at 1C activation energy	Fitted
$J_{0,ref}$	0.1	—	Dimensionless charge exchange current pre-exponential factor	Fitted
Ea_{J0}	$-14 \cdot 10^{3}$	J mol^{-1}	Dimensionless charge exchange current activation energy	Fitted
Ea_{τ}	$12 \cdot 10^{3}$	J mol^{-1}	Diffusion time-constant activation energy	Fitted
τ_{ref}	$1 \cdot 10^{3}$	s	Diffusion time-constant pre-exponential factor	Fitted
I_{1C}	3	A	Current corresponding to 1C	Fitted
Q_{actual}	$10.8 \cdot 10^{3}$	C	Cell capacity as rated by the supplier	Measured
SoC_0	1	—	Initial state of charge	Measured
t_{epoxy}	$1.524 \cdot 10^{-4}$	m	Thickness of the epoxy layer	Measured
hs_{height}	$8.7452 \cdot 10^{-2}$	m	Height of the heat sink	Measured
$hs_{thickness}$	$7.6424 \cdot 10^{-3}$	m	Thickness of the heat sink	Measured
dz_{cells}	$8.128 \cdot 10^{-4}$	m	Clearance between the cell cans in the z-direction	Measured
dx_{cells}	$2.0574 \cdot 10^{-2}$	m	Space between the centers of the cells in the x-direction	Measured
dx_{c-hs}	$1.0287 \cdot 10^{-2}$	m	Space between the heat sink center and the center of the cells in the x-direction	Measured
$k_x = k_z$	3.4	W m^{-1} K^{-1}	Cross-plane (radial) cells thermal conductivity	34
k_y	20	W m^{-1} K^{-1}	In-plane (axial) cells thermal conductivity	34
k_{epoxy}	0.391	W m^{-1} K^{-1}	Thermal conductivity of the Epoxy layer	43
ρ_{eff}	$2.7 \cdot 10^{3}$	kg m^{-3}	Effective density of the cell	34
$C_{p,eff}$	$1.28 \cdot 10^{3}$	J kg^{-1} K^{-1}	Effective heat capacity of the cell	34
k_{Al6061}	167	W m^{-1} K^{-1}	Thermal conductivity of the heat sink	44
ρ_{Al6061}	$2.7 \cdot 10^{3}$	kg m^{-3}	Density of the heat sink	44
$C_{p,Al6061}$	896	J kg^{-1} K^{-1}	Heat capacity of the heat sink	44
I	−9.6	A	Applied constant current	Measured

ORCID

Paul T. Coman https://orcid.org/0000-0003-2876-7441
Eric C. Darcy https://orcid.org/0000-0002-8426-8607

References

1. J. Newman and T.-A. E. Karen, *Electrochemical Systems.* (Wiley, New Jersey, NJ) 3rd ed. (2004).
2. J. Newman and W. Tiedemann, "Porous-electrode theory with battery applications." *AIChE J.*, **21**, 25 (1975).
3. T. F. Fuller and J. Newman, *Relaxation Phenomena in Lithium-ion-Insertion Cells.*, **141**982 (1994).
4. M. Doyle, J. Newman, A. S. Gozdz, C. N. Schmutz, and J.-M. M. Tarascon, "Comparison of modeling predictions with experimental data from plastic lithium ion cells." *J. Electrochem. Soc.*, **143**, 1890 (1996).
5. C. Li, N. Cui, C. Wang, and C. Zhang, "Reduced-order electrochemical model for lithium-ion battery with domain decomposition and polynomial approximation methods." *Energy*, **221**, 119662 (2021).
6. L. Wu, K. Liu, and H. Pang, "Evaluation and observability analysis of an improved reduced-order electrochemical model for lithium-ion battery." *Electrochim. Acta*, **368**, 137604 (2021).
7. K. A. Smith, C. D. Rahn, and C. Y. Wang, "Model order reduction of 1D diffusion systems via residue grouping." *J. Dyn. Syst. Meas. Control. Trans. ASME*, **130**, 0110121 (2008).
8. M. Seo, Y. Song, J. Kim, S. W. Paek, G. H. Kim, and S. W. Kim, "Innovative lumped-battery model for state of charge estimation of lithium-ion batteries under various ambient temperatures." *Energy*, **226**, 120301 (2021).
9. Z. Chu, G. L. Plett, M. S. Trimboli, and M. Ouyang, "A control-oriented electrochemical model for lithium-ion battery, part i: lumped-parameter reduced-order model with constant phase element." *J. Energy Storage*, **25**, 100828 (2019).
10. M. Guo and R. E. White, "Thermal model for lithium ion battery pack with mixed parallel and series configuration." *J. Electrochem. Soc.*, **158**, A1166 (2011).
11. E. Prada, D. D. Domenico, Y. Creff, J. Bernard, V. Sauvant-Moynot, and F. Huet, "Simplified electrochemical and thermal model of $LiFePO_4$-graphite li-ion batteries for fast charge applications." *J. Electrochem. Soc.*, **159**, A1508 (2012).
12. G. Fan, X. Li, and M. Canova, "A reduced-order electrochemical model of li-ion batteries for control and estimation applications." *IEEE Trans. Veh. Technol.*, **67**, 76 (2018).
13. X. Li, G. Fan, G. Rizzoni, M. Canova, C. Zhu, and G. Wei, "A simplified multi-particle model for lithium ion batteries via a predictor-corrector strategy and quasi-linearization." *Energy*, **116**, 154 (2016).
14. S. K. Rahimian, S. Rayman, and R. E. White, "Comparison of single particle and equivalent circuit analog models for a lithium-ion cell." *J. Power Sources*, **196**, 8450 (2011).
15. J. Gomez, R. Nelson, E. E. Kalu, M. H. Weatherspoon, and J. P. Zheng, "Equivalent circuit model parameters of a high-power Li-ion battery: Thermal and state of charge effects." *J. Power Sources*, **196**, 4826 (2011).
16. K. S. Hariharan and V. Senthil Kumar, "A nonlinear equivalent circuit model for lithium ion cells." *J. Power Sources*, **222**, 210 (2013).
17. A. Farmann and D. U. Sauer, "Comparative study of reduced order equivalent circuit models for on-board state-of-available-power prediction of lithium-ion batteries in electric vehicles." *Appl. Energy*, **225**, 1102 (2018).
18. Y. Saito, K. Takano, and A. Negishi, "Thermal behaviors of lithium-ion cells during overcharge." *J. Power Sources*, **97–98**, 693 (2001).
19. X. Hu, S. Li, and H. Peng, "A comparative study of equivalent circuit models for Li-ion batteries." *J. Power Sources*, **198**, 359 (2012).
20. S. Li et al., "Optimal cell tab design and cooling strategy for cylindrical lithium-ion batteries." *J. Power Sources*, **492**, 229594 (2021).
21. H. Ekström, B. Fridholm, and G. Lindbergh, "Comparison of lumped diffusion models for voltage prediction of a lithium-ion battery cell during dynamic loads." *J. Power Sources*, **402**, 296 (2018).
22. B. Ng, P. T. Coman, W. E. Mustain, and R. E. White, "Non-destructive parameter extraction for a reduced order lumped electrochemical-thermal model for simulating Li-ion full-cells." *J. Power Sources*, **445** (2020).
23. V. Pizarro-Carmona, S. Castano-Solís, M. Cortés-Carmona, J. Fraile-Ardanuy, and D. Jimenez-Bermejo, "GA-based approach to optimize an equivalent electric circuit model of a Li-ion battery-pack." *Expert Syst. Appl.*, **172**, 1 (2021).
24. F. Kolodziejczyk, B. Mortazavi, T. Rabczuk, and X. Zhuang, "Machine learning assisted multiscale modeling of composite phase change materials for Li-ion batteries' thermal management." *Int. J. Heat Mass Transf.*, **172**, 121199 (2021).
25. D. Kang, P. Y. Lee, K. Yoo, and J. Kim, "Internal thermal network model-based inner temperature distribution of high-power lithium-ion battery packs with different shapes for thermal management." *J. Energy Storage*, **27**, 101017 (2020).
26. Z. Y. Jiang, Z. G. Qu, J. F. Zhang, and Z. H. Rao, "Rapid prediction method for thermal runaway propagation in battery pack based on lumped thermal resistance network and electric circuit analogy." *Appl. Energy*, **268**, 115007 (2020).
27. K. E. Thomas and J. Newman, "Thermal modeling of porous insertion electrodes." *J. Electrochem. Soc.*, **150**, A176 (2003).
28. A. Amini, T. Özdemir, Ö. Ekici, S. Ç. Başlamışlı, and M. Köksal, "A thermal model for Li-ion batteries operating under dynamic conditions." *Appl. Therm. Eng.*, **185**, 116338 (2021).
29. K. H. Kwon, C. B. Shin, T. H. Kang, and C. S. Kim, "A two-dimensional modeling of a lithium-polymer battery." *J. Power Sources*, **163**, 151 (2006).

30. H. Gu, "Mathematical Analysis of a Zn/NiOOH Cell." *J. Electrochem. Soc.*, **130**, 1459 (1983).
31. S. Chacko and Y. M. Chung, "Thermal modelling of Li-ion polymer battery for electric vehicle drive cycles." *J. Power Sources*, **213**, 296 (2012).
32. V. V. Ganesan and A. Jain, "Computationally-efficient thermal simulations of large Li-ion battery packs using submodeling technique." *Int. J. Heat Mass Transf.*, **165**, 120616 (2021).
33. E. C. Darcy et al., "Safe, high power/voltage battery design challenges." in*NASA Aerospace Battery Workshop* (NASA) 1 (2019).
34. H. Maleki, S. A. Hallaj, J. R. Selman, R. B. Dinwiddie, and H. Wang, "Thermal properties of lithium-ion battery and components." *J. Electrochem. Soc.*, **146**, 947 (1999).
35. P. T. Coman, E. C. Darcy, C. T. Veje, and R. E. White, "Modelling Li-ion cell thermal runaway triggered by an internal short circuit device using an efficiency factor and Arrhenius formulations." *J. Electrochem. Soc.*, **164**, A587 (2017).
36. C. Bost, (2020), COMSOL Blog - Modeling Heat Transfer in Thin Layers via Layered Material Technology Available at: (https://comsol.com/blogs/modeling-heat-transfer-in-thin-layers-via-layered-material-technology/). (Accessed: 5th May 2021).
37. M. Guo, X. Jin, and R. E. White, "Nonlinear state-variable method for solving physics-based li-ion cell model with high-frequency inputs." *J. Electrochem. Soc.*, **164**, E3001 (2017).
38. M. Song, Y. Hu, and S.-Y. Choe, "Analysis and Measurement of Heat Sources of Lithium-Ion Polymer Battery Using Electrochemical Thermal Model and Calorimeter." *NASA Aerospace Battery Workshop*, Huntsville, Alabama, Nov. 20, 2019 (2019).
39. F. Elmahdi, L. Ismail, and M. Noureddine, "Fitting the OCV-SOC relationship of a battery lithium-ion using genetic algorithm method." *E3S Web Conf.*, **234**, 3 (2021).
40. S. Ma, M. Jiang, P. Tao, C. Song, J. Wu, J. Wang, T. Deng, and W. Shang, "Temperature effect and thermal impact in lithium-ion batteries: A review." *Prog. Nat. Sci. Mater. Int.*, **28**, 653 (2018).
41. D. Ren, K. Smith, D. Guo, X. Han, X. Feng, L. Lu, M. Ouyang, and J. Li, "Investigation of lithium plating-stripping process in Li-ion batteries at low temperature using an electrochemical model." *J. Electrochem. Soc.*, **165**, A2167 (2018).
42. M. Guo, G. Sikha, and R. E. White, "Single-Particle Model for a Lithium-Ion Cell: Thermal Behavior." *J. Electrochem. Soc.*, **158**, A122 (2011).
43. V. D. McGinniss, F. A. Sliemers, D. K. Lmdstrom, and S. G. Talbert, "Compendium Of information on identification and testing of materials for plastic solar thermal collectors." *US Department of Energy*, **9**, 1 (1980).
44. P. T. Coman, E. C. Darcy, C. T. Veje, and R. E. White, "Numerical analysis of heat propagation in a battery pack using a novel technology for triggering thermal runaway." *Appl. Energy*, **203**, 189 (2017).